The Role of Internal Tides in Mixing the Deep Ocean

LOUIS ST. LAURENT AND CHRIS GARRETT

School of Earth and Ocean Sciences, University of Victoria, Victoria, British Columbia, Canada

(Manuscript received 30 November 2000, in final form 5 April 2002)

ABSTRACT

Internal wave theory is used to examine the generation, radiation, and energy dissipation of internal tides in the deep ocean. Estimates of vertical energy flux based on a previously developed model are adjusted to account for the influence of finite depth, varying stratification, and two-dimensional topography. Specific estimates of energy flux are made for midocean ridge topography. Weakly nonlinear theory is applied to the wave generation at idealized topography to examine finite amplitude corrections to the linear theory. Most internal tide energy is generated at low modes associated with spatial scales from roughly 20 to 100 km. The Richardson number of the radiated internal tide typically exceeds unity for these motions, and so direct shear instability of the generated waves is not the dominant energy transfer mechanism. It also seems that wave–wave interactions are ineffective at transferring energy from the large wavelengths that dominate the energy flux. Instead, it appears that most of the internal tide energy is radiated over O(1000 km) distances. A small fraction of energy flux, less than 30%, is generated at smaller spatial scales, and this energy flux may dissipate locally. Estimates along the Mid-Atlantic Ridge in the South Atlantic suggest that the vertical energy flux of M_2 internal tides is 3–5 mW m^{-2}, with 1–2 mW m^{-2} likely contributing to local mixing. Along the East Pacific Rise, bathymetry is more smooth and tides are weaker, and estimates suggest internal tide energy flux is negligible. Radiated low modes are likely influenced by topographic scattering, though general topography scatters less than 10% of the low-mode energy to higher wavenumbers. Thus, low-mode internal tides may contribute to mixing at locations far away from their generation sites.

1. Introduction

Breaking internal waves are the main cause of diapycnal mixing in the ocean. They may be generated by wind at the sea surface or by flow over the topography of the seafloor. While mean flows and eddy activity in the deep ocean are characterized by O(1 mm s^{-1}) currents, barotropic tidal currents in the deep ocean are O(10 mm s^{-1}) and may be an important source of internal waves. Munk and Wunsch (1998) review the evidence suggesting that tides do about 3.7 TW of work on the global ocean, with 2.5 TW contributed by the semidiurnal lunar tides. Egbert and Ray (2000, 2001) have examined least squares fits of models for the global barotropic tide to TOPEX/Poseidon altimetry data, and they interpret model residuals in terms of ''tidal dissipation.'' In Egbert and Ray's studies, dissipation refers to any mechanisms that transfer energy away from the barotropic tide: they are not able to distinguish whether barotropic energy is lost to baroclinic waves (the internal tide) or to bottom friction. Egbert and Ray (2000, 2001) estimate that up to 1 TW of power is lost from barotropic tides in the deep ocean. Frictional dissipation can be estimated from the relation $\rho c_d |u| u^2$, where $c_d = 0.0025$ is the drag coefficient. For typical open-ocean tidal speeds, $u \simeq 0.03$ m s^{-1}, the frictional dissipation is less than 0.1 mW m^{-2}. Globally, this accounts for less than 30 GW of barotropic tidal power loss. Thus, nearly all barotropic power conversion in the deep ocean must occur as internal tides.

Egbert and Ray (2000, 2001) identify a number of deep ocean regions where barotropic tidal energy is likely being transferred to internal tides. These regions are generally associated with three types of topography: (i) oceanic islands, (ii) oceanic trenches, and (iii) midocean ridges. Oceanic islands such as Hawaii, and oceanic trenches such as those in the west Pacific Ocean, are steep topographic features with typical slope s (rise over run) from 0.1 to 0.3 (Seibold and Berger 1996). Egbert and Ray (2000, 2001) identify the oceanic islands of Micronesia and Melanesia as sites accounting for over 100 GW of internal tide production, while Hawaii accounts for 20 GW. They also identify midocean ridge topography in the Atlantic and Indian Oceans as each accounting for over 100 GW of internal tide production. These topographic features have slopes that vary over a wide range of spatial scales.

Corresponding author address: Louis C. St. Laurent, Department of Oceanography, The Florida State University, Tallahassee, FL 32306.
E-mail: lous@ocean.fsu.edu

Observations of internal tides and mixing

The contribution of internal tides to oceanic velocity and temperature records has long been recognized. Wunsch (1975) and Hendershott (1981) present reviews of earlier work. Renewed interest in internal tides came with observations of sea surface elevation by the TOPEX/Poseidon altimeter. These data have been used to constrain hydrodynamic models of the tides, and hence produce accurate estimates of open-ocean barotropic tides (Egbert et al. 1994; Egbert 1997). A multiyear record of observations is now available, and the semidiurnal tides (M_2 and S_2) can be dealiased from the record. Ray and Mitchum (1996) used along-track TOPEX/Poseidon records to examine the surface manifestation of internal tides generated along the Hawaiian Islands. They found that both first and second baroclinic modes of the semidiurnal internal tides were present in the data and that the signal of internal tide propagation could be tracked up to 1000 km away from the Hawaiian Ridge. In a further analysis of the altimetry data, Ray and Mitchum (1997) estimate that 15 GW of semidiurnal internal tide energy radiates away from the Hawaiian Ridge in the first baroclinic mode. TOPEX/Poseidon altimetry records have also been used by Cummins et al. (2001) to show that internal tides generated at the Aleutian Ridge can be tracked over 1000 km into the central Pacific, though the total internal tide energy flux is only about 2 GW.

Microstructure observations have provided direct observations of mixing driven by internal tides at steep topography (Lueck and Mudge 1997; Kunze and Toole 1997; Lien and Gregg 2001). Lueck and Mudge (1997) attributed enhanced turbulence at Cobb Seamount in the northeast Pacific to a semidiurnal internal tide. They found that the largest turbulence levels occurred along a beam of internal tide energy emanating from the seamount rim. Kunze and Toole (1997) describe microstructure observations from Fieberling Seamount in the northeast Pacific. They found the largest mixing levels at the summit of the seamount where diurnal internal tide energy was trapped. Internal tides are also produced along the continental margins of the ocean basins, and evidence of internal-tide-driven mixing at Monterey Canyon off California was reported by Lien and Gregg (2001). They found enhanced turbulence levels along the ray path of a semidiurnal internal tide beam extending out to a distance of 4 km away from the topography.

Evidence of internal-tide-driven mixing from the truly deep ocean was found during the Brazil Basin Tracer Release Experiment (Polzin et al. 1997; Ledwell et al. 2000). This study was conducted near the Mid-Atlantic Ridge. St. Laurent et al. (2001) present vertically integrated dissipation data that are modulated over the spring–neap tidal cycle with a small lag of about a day. Maximum levels of dissipation, vertically integrated to 2000 m above the bottom, reach 3 mW m^{-2}. These observations span a network of fracture zones west of the Mid-Atlantic Ridge, with topographic relief varying by up to 1 km between the crests and floors of abyssal canyons. The dominant topography of the fracture zone system has a slope less than 0.1 as the canyons are generally 30–50 km wide. Elevated turbulent dissipation rates were found along all regions of the fracture zone topography, but turbulence levels appeared most enhanced over the slopes. Above all classes of topography, turbulence levels decrease to background levels at heights above bottom greater than about 1000 m.

The energy flux carried by the internal tide can radiate as propagating internal waves, and these waves are subject to a collection of processes that will eventually lead to dissipation. Shear instability, wave–wave interactions, and topographic scattering all act to influence the rate of dissipation and control whether the internal tide dissipates near the generation site or far away.

In this paper we will review several issues relevant to the role of internal tides in mixing the deep ocean. In particular, we consider the following questions. What is the shape of the energy flux spectrum? Is the generated internal tide stable to shear instability? How efficient are wave–wave interactions at modifying the internal-tide spectrum? What causes the internal tides to dissipate? Are internal tides likely to dissipate near their generation sites or far away? In section 2, we discuss some linear theory for the internal tide and present a calculation of internal tide energy flux. The nondimensional parameters that define the wave response to flow over topography are discussed, and the energy-flux spectrum is described. The effects of finite depth and variable stratification are discussed in section 2a. Calculations of energy flux at midocean ridge topography are presented in section 2b. Energy flux production along steeper topography is considered in section 2c. In section 3, we discuss issues related to the radiation and dissipation of internal tides. We consider the stability of the internal tide to shear (section 3a), and the influence of wave–wave interactions (section 3b). The influence of topographic scattering on the internal tide spectrum is considered in section 3c. Finally, some implications for mixing are discussed in section 4.

2. Internal tide energy flux

Internal tides are produced in stratified regions where barotropic tidal currents flow over topography. Internal tides radiate throughout the oceans with frequencies identical to those of the barotropic tides (M_2, S_2, O_1, K_1, etc.) and their harmonics, provided the frequency ω falls in the range $f < \omega < N$. Poleward of the inertial latitudes where $\omega = f$, internal tides are trapped over topography. Thus, while internal tides of diurnal frequency can only propagate freely equatorward of about $\pm 30°$ latitude, semidiurnal tides are freely propagating throughout most of the ocean, as $\omega_{M_2} = |f|$ at $\pm 74.5°$ latitude.

For a given wavenumber component k of topography

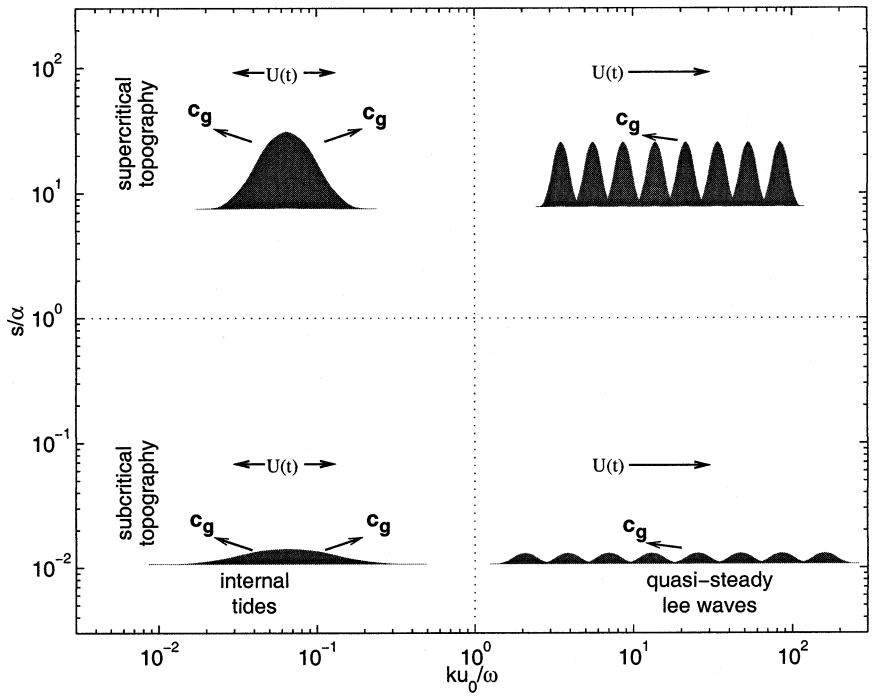

FIG. 1. Diagram showing the internal wave response to tidal flow over bathymetry for the slope parameter s/α and the tidal excursion parameter ku_0/ω. Internal tides occur when the scale of the topography k^{-1} exceeds the tidal excursion scale u_0/ω. In this regime, waves radiate energy in both the up- and downstream directions [as shown by the group velocity (c_g) vectors]. Quasi-steady lee waves occur when the scale of tidal excursion exceeds the scale of the topography. Wave energy is radiated in the upstream direction only.

with amplitude a, four nondimensional parameters characterize the deep-ocean internal waves generated by the tidal current with amplitude u_0. Two parameters, ω/f and ω/N, specify the timescale of the tide relative to the inertial and buoyancy timescales. The two additional parameters are dynamically more significant, and a diagram showing the various regimes defined by these additional parameters is shown in Fig. 1. One of these parameters, ku_0/ω, measures the ratio of the tidal excursion amplitude u_0/ω to the horizontal scale of the bathymetry k^{-1}. This parameter also measures the ratio of the barotropic tidal speed u_0 to the wave speed ω/k. The remaining parameter, ka/α, measures the ratio of topographic slope $s = ka$ to the slope α of a radiated tidal beam,

$$\alpha = \frac{k}{m} = \left(\frac{\omega^2 - f^2}{N^2 - \omega^2}\right)^{1/2}. \tag{1}$$

We also note that ka/α may be expressed as ma, the ratio of the topographic amplitude to the vertical scale of the internal waves.

The tidal excursion parameter serves to classify two regimes of interest. In one regime, the tidal excursion is less than the scale of the bathymetry. The waves of this ''internal tide'' regime radiate mainly at the fundamental frequency of the tide in both the up- and downstream directions. In the other regime, the tidal excursion exceeds the length scale of the bathymetry. This is referred to as the ''quasi-steady lee wave'' regime, with waves that propagate only in the upstream direction with frequencies $-kU(t)$ and phase speeds $-U(t)$. Higher harmonic internal tides manifest themselves mainly as quasi-steady lee waves.

The steepness parameter, s/α, is also used to distinguish two regimes. Topography is referred to as ''supercritical'' when its slope is greater than the slope of a tidal beam ($s/\alpha > 1$), while ''subcritical'' topography has slope less steep than a tidal beam ($s/\alpha < 1$). Using (1) with $\omega = 1.4 \times 10^{-4}$ s^{-1}, $N = 1 \times 10^{-3}$ s^{-1}, and $f = 1 \times 10^{-4}$ s^{-1}, $\alpha \simeq 0.10$ provides a reference value for the slope of an M_2 tidal beam in the deep ocean. It follows that many oceanic island and trench features are supercritical, while large-scale features of midocean ridge topography are subcritical.

The equations for supercritical topography are reviewed by Baines (1982), and solutions for specific topographic geometries can be computed using ray tracing methods. Solutions for ridge, slope, and shelf topography have been discussed by Rattray (1960), Baines (1982), and Craig (1987). A simplified model for internal tide generation at a topographic step was proposed by Stigebrandt (1980) and applied to deep ocean topographies by Sjöberg and Stigebrandt (1992). However, the equations for arbitrary supercritical topography

$h(\mathbf{x})$ are difficult to solve due to the necessity of a nonlinear bottom boundary condition, $w(h) = \mathbf{U}\cdot\nabla h + \mathbf{u}\cdot\nabla h$, where $\mathbf{U}$ is the barotropic current vector and ($\mathbf{u}$, w) are the lateral and vertical components of the baroclinic velocity. The baroclinic wave response to barotropic tidal flow over arbitrary steep topography has instead been studied using numerical simulations. In particular, numerical studies have been carried out for internal tides at the Hawaiian Ridge (Holloway and Merrifield 1999; Merrifield et al. 2001) and the Aleutian Ridge (Cummins et al. 2001). Simulations of internal tide generation at steep idealized topographies are presented by Li (2002, manuscript submitted to *J. Mar. Res.*) and Khatiwala (2002, manuscript submitted to *Deep-Sea Res.*) The properties of quasi-steady lee waves have also been studied numerically for atmospheric (Lott and Teitelbaum 1993) and oceanographic (Nakamura et al. 2000) cases.

Models for internal tide generation by subcritical topography have been developed by Cox and Sandstrom (1962), Baines (1973), Bell (1975a,b), Hibiya (1986), and Llewellyn Smith and Young (2002). These models apply a linearized bottom boundary condition $w(-H) = \mathbf{U}\cdot\nabla h$. Two approximations are made in this linearization: (i) the neglect of the term $\mathbf{u}\cdot\nabla h$ involving the lateral current vector $\mathbf{u}$ of the internal tide and (ii) the use of a constant depth $z = -H$ in place of $z = h(\mathbf{x})$ in applying the boundary condition. Both of these approximations are justified when the slope parameter satisfies $s/\alpha \ll 1$. With application of the linear boundary condition, solutions for arbitrary bathymetry can be obtained by superposition.

Bell (1975a,b) considered internal waves generated at subcritical topography in an ocean of infinite depth. His theory is applicable in both the internal tide and quasi-steady lee wave regimes. The vertical energy flux E_f is a quantity of primary interest for studies of mixing. This quantity is often expressed as a work quantity $E_f = \langle pw \rangle$ for the wave pressure p, or as the product $E_f = c_g E_d$ between the vertical group speed c_g and the wave energy E_d. Bell's expression for the phase-averaged energy flux produced along bathymetry with a (one sided) power spectrum $\phi(k)$ is

$$E_f = 2\rho_0 \sum_{n=1}^{n_N} n\omega[(N_b^2 - n^2\omega^2)(n^2\omega^2 - f^2)]^{1/2} \times \int_0^\infty k^{-1} J_n^2\left(\frac{ku_0}{\omega}\right)\phi(k)\, dk, \quad (2)$$

where N_b is the buoyancy frequency along the bottom and J_n is the Bessel function. The index n corresponds to tidal harmonics, with the maximum harmonic n_N being the largest integer less than N_b/ω. In (2), the power spectrum is normalized to satisfy $\int_0^\infty \phi(k)\, dk = \overline{h^2}$, where $\overline{h^2}$ is the mean square height of the topography.

It is useful to examine the approximate limiting forms of the Bessel function in (2), which are $J_n \simeq [(ku_0)/(2\omega)]^n/n!$ for $ku_0/\omega \ll 1$, and $J_n \simeq \sqrt{(2\omega/\pi ku_0)}\cos(ku_0/\omega - n\pi/2 - \pi/4)$ for $ku_0/\omega \gg 1$. In the later expression, the cosine term represents the constructive and destructive interference between quasi-steady lee waves generated during successive tidal periods. The approximate wavenumber dependence of the energy flux for the internal tide of fundamental frequency ($n = 1$) is $k\phi(k)$ for $ku_0/\omega < 1$, and $k^{-2}\phi(k)$ for $ku_0/\omega > 1$. Thus, the spectrum of energy flux is more "blue" than the bathymetric spectrum in the internal-tide regime and more "red" in the quasi-steady lee wave regime. For the common case of small tidal excursion, the energy flux is well approximated by

$$E_f = \frac{1}{2}\rho_0 \frac{[(N_b^2 - \omega^2)(\omega^2 - f^2)]^{1/2}}{\omega} \int_0^\infty ku_0^2 \phi(k)\, dk. \quad (3)$$

a. Equivalent modes and finite depth

The integration in (2) is performed over a continuous spectrum of wavenumbers. In Bell's theory, the internal waves radiated away from topography are assumed to never reach the upper ocean, where the waves would reflect at the upper surface. This assumption is justified if the internal waves are dissipated rapidly after generation. For waves that are not rapidly dissipated, the neglect of upper-ocean reflection is justified only in an ocean of infinite depth.

In finite depth formulations, the internal tide response is modeled as baroclinic modes. The modal dispersion relation given by

$$k_j = \frac{j\pi}{H}\left(\frac{\omega^2 - f^2}{\overline{N}^2 - \omega^2}\right)^{1/2}, \quad (4)$$

where $j = 1, 2, 3, \ldots$; $\delta k = (\pi/H)\,[(\omega^2 - f^2)/(\overline{N}^2 - \omega^2)]^{1/2}$ is the spacing between modes, and H is the depth. Hibiya (1986) derived (4) for the case of constant N with $f = 0$. Llewellyn Smith and Young (2002) show that (4) is a valid approximation for the case of a depth-varying stratification when $\overline{N}$ is taken as the depth-averaged stratification, $\overline{N} = (1/H)\int_{-H}^{0} N(z)\, dz$. In the finite depth derivations, the integral over continuous wavenumbers in (2) is replaced by a summation over discrete modes, though this sum tends to (2) as the ocean depth tends to infinity.

The primary influence of finite depth on the internal tide energy flux is that the largest scale of internal wave response is limited to that of the mode-1 wave. This suggests that using $k_0 = k_1 - \frac{1}{2}\delta k$ as the lower limit of integration in (2) provides the first-order finite depth correction to Bell's theory. The magnitude of this correction to the energy flux estimate depends on the shape of the bathymetric spectrum $\phi(k)$, with the correction being largest for spectra that are red at low wavenumbers. There is additional inaccuracy in (2) that arises when doing a continuous integration over wavenumbers instead of a discrete sum over modes. In practice, this

amounts to only a small error in the integrated estimate of energy flux.

In the calculations that follow, we will integrate (2) from k_0 to ∞ and refer to the wavenumbers given by (4) as ''equivalent modes.'' This term signifies that the internal-tide response at a given wavenumber k_j may never occur as an actual baroclinic mode. This is particularly true for the internal tides generated at high wavenumbers, which may dissipate before ever reaching the upper ocean. However, by referring to equivalent modes, we may easily refer to a given wavenumber portion of the internal-tide spectrum.

b. *Energy flux estimates for midocean ridge topography*

1) TOPOGRAPHY IN ONE DIMENSION

Here, we consider internal tides generated at midocean ridge topography. We anticipate that the dominant wavelengths of midocean ridge topography will have subcritical slopes, justifying the use of subcritical theory. We will use Bell's (1975a,b) theory to estimate the energy flux according to (2), using $k_0 = k_1 - \frac{1}{2}\delta k$ as the lower limit of integration.

It has long been established that the roughness of midocean ridge topography varies according to the spreading rates of the seafloor (Small and Sandwell 1992). In general, the roughness and steepness of ridge topography are inversely proportional to the spreading rate of the seafloor. To examine the likely range of energy flux production at midocean ridges, we consider topography from two regions. An example of fast-spreading seafloor topography is taken from a region of the East Pacific Rise (EPR) near (17°S, 115°W), just south of the Garrett Fracture Zone. An example of slow-spreading seafloor topography is taken from a region of the Mid-Atlantic Ridge (MAR) near (27°S, 14°W), just north of the Rio Grande Fracture Zone. These two regions are useful, as they represent extreme cases. Multibeam bathymetry data for these regions are available from the RIDGE Multibeam Synthesis Project, and maps showing the data are presented in Fig. 2. Sections of multibeam data have 200-m resolution in the lateral directions.

Bathymetric spectra from these regions were computed along several sections of the multibeam data (Fig. 3). The spectra have been normalized such that the integrated spectrum gives the mean square height of topography, $\int_0^\infty \phi(k)\, dk = \overline{h^2}$. For each region, spectra were computed both across the direction of fracture zones (XFZ) and along the direction of fracture zones (FZ). At large horizontal wavelengths ($2\pi k^{-1} > 10$ km), the crest and canyon bathymetry of the fracture zones are the dominant topography. This is evident in the spectra, as the XFZ spectra dominate over the FZ spectra at large wavelengths. At smaller wavelengths ($2\pi k^{-1} <$ 10 km) abyssal hills are the dominant mode of topography (Goff 1991). These occur primarily in the FZ direction, and their signal is evident in the FZ spectrum from the MAR (Fig. 3b). In both EPR and MAR cases, the XFZ spectra contain roughly twice the variance of the FZ spectra.

Slope spectra follow directly from the bathymetric spectra as $k^2\phi(k)$, and the slope spectra for the across FZ bathymetry are also shown in Fig. 3. The mean square slope ($\overline{s^2}$) at any wavenumber k can be calculated by integrating the slope spectrum,

$$\overline{s(k)^2} = \int^k k'^2 \phi(k')\, dk'. \tag{5}$$

In general, there will exist some wavenumber k_c where $s(k_c) = \alpha$, the slope corresponding to critical generation of a tidal beam. The topographic slopes on wavelengths greater than $2\pi k_c^{-1}$ are subcritical, while the topographic slopes on wavelengths less than $2\pi k_c^{-1}$ are supercritical. The possible range of critical slope wavenumbers for the EPR and MAR data is shown in Fig. 3. These wavenumbers correspond to topography with horizontal wavelengths of roughly 1 km.

The length scale corresponding to the amplitude of the tidal excursion u_0/ω is an additional important parameter, requiring estimates of the tidal velocities. Barotropic tidal velocity data for the EPR and MAR sites considered here were produced using the TPXO.3 global tidal model (Egbert et al. 1994; Egbert 1997) for the year between 1 January 2000 and 1 January 2001. Records of barotropic tidal currents (U, V) were produced at 2° Mercator intervals spanning the bathymetric sections. The M_2 components of these records were extracted, and tidal ellipses were computed using standard methods (e.g., Godin 1972). The spatially averaged M_2 tidal ellipses for each site are shown in Fig. 4. Current amplitudes along the semimajor and semiminor axes of the ellipses were projected onto the FZ and XFZ directions to give estimates of u_0 for use in the energy flux calculations. Current amplitudes along the EPR bathymetry are (0.010, 0.008) m s^{-1} for the (FZ, XFZ) directions, respectively. The corresponding current amplitudes for the MAR bathymetry are (0.031, 0.026) m s^{-1}. Tidal excursion amplitudes in the XFZ directions are 53 m and 185 m for the EPR and MAR sites, respectively.

Topographic slopes on wavelengths greater than 1 km are subcritical. Therefore, we assume that theory for subcritical topography is applicable, and we use the spectra of XFZ bathymetry shown in Fig. 3 with expression (2) to calculate energy flux spectra. The fine spatial resolution of these one-dimensional sections allow us to examine the spectrum of energy flux to very large equivalent modes.

For these calculations, stratification data provides both the bottom value of buoyancy frequency in (2), and also the buoyancy scaling for the modal dispersion relation (4). Buoyancy frequency profiles for the EPR

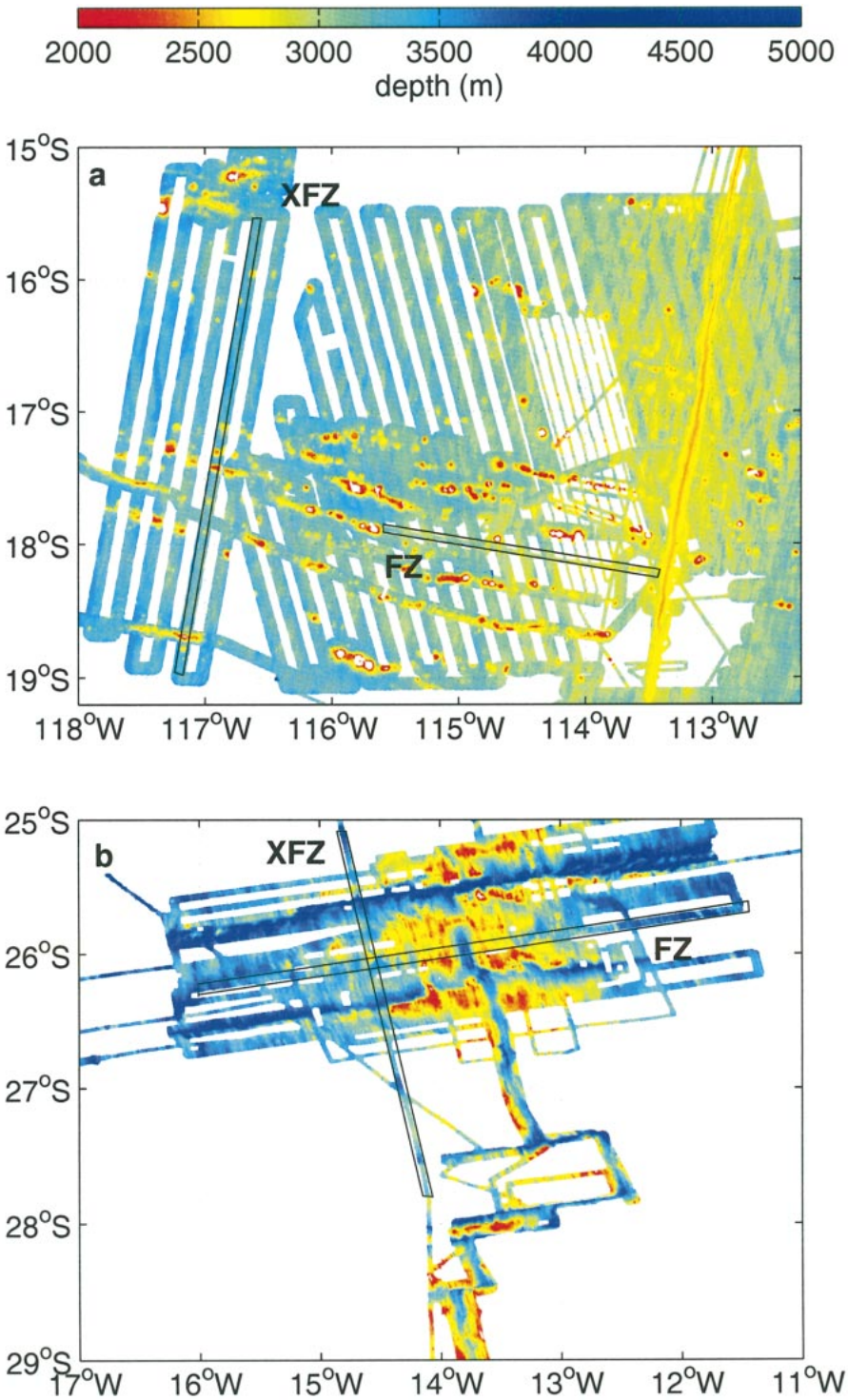

FIG. 2. Multibeam bathymetry data from the (a) EPR and (b) MAR. Bathymetric sections were taken along fracture zones (FZ) and across fracture zones (XFZ) to calculate spectra. Boxed regions indicate the locations of several sections described in the text.

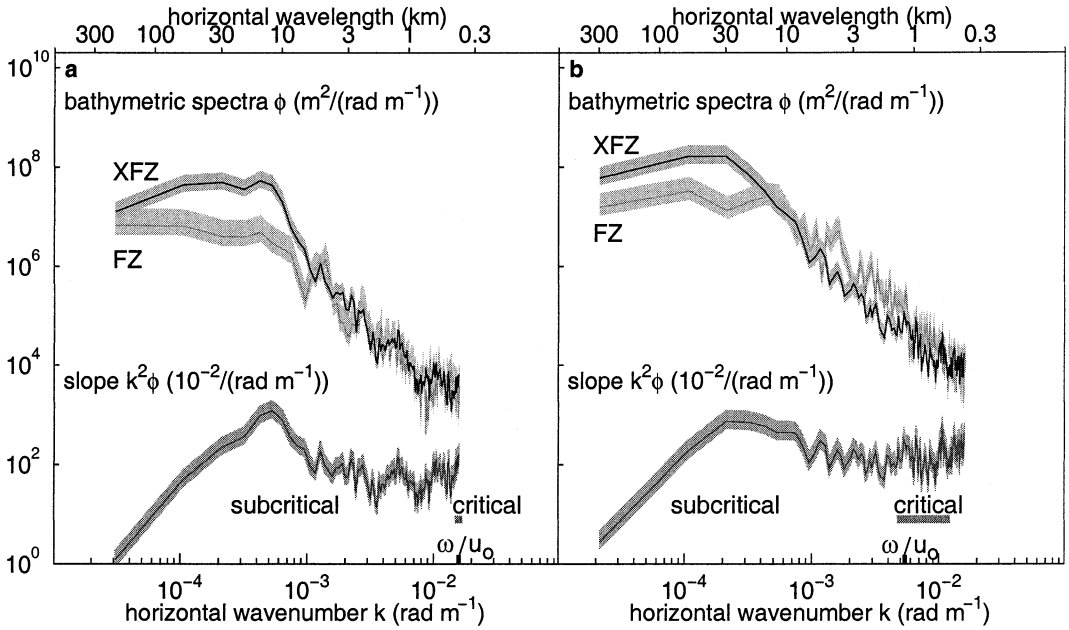

FIG. 3. Bathymetric spectra for the (a) EPR and (b) MAR from sections shown in Fig. 2. The standard deviations of the spectral estimates are represented by the shaded bands. In each panel, the slope spectra of the XFZ bathymetry are also shown. The wavenumber of the tidal excursion scale ω/u_0 is shown for each site. The range of wavenumbers associated with subcritical and critical slopes for each XFZ spectrum is indicated.

and MAR regions are shown in Fig. 5. These profiles were derived from temperature and salinity data from the Levitus et al. (1994) and Levitus and Boyer (1994) database, and approximate fits to each profile are shown in the figure. An exponential profile $N = N_0 \exp(z/b)$ with $N_0 = 0.005\,24\ \text{s}^{-1}$ and $b = 1300$ m was used for the stratification at the EPR site. An offset of $N_1 = 0.0005\ \text{s}^{-1}$ was added to the exponential dependence to account for the contrast between North Atlantic Deep Water and Antarctic Bottom Water below 3000 m at the MAR site. While these simple fits have rather poor fidelity at any given depth, they do capture the general structure of the stratification, and thus provide the basis for an estimate of $\overline{N}$ for use in (4). For the exponential fit with the offset, the equivalent mode dispersion relation can be approximated as

$$k_j = \frac{j\pi(\omega^2 - f^2)^{1/2}}{N_0 b + N_1 H}, \tag{6}$$

where the denominator was taken as $(\overline{N}^2 - \omega^2)^{1/2} H \approx \overline{N} H$ since $\overline{N}^2 \gg \omega^2$. In the case of an exponential stratification with no offset (EPR case), the dispersion relation (6) has no dependence on the depth H.

Energy flux estimates were made using frequency parameters $\omega = 1.4 \times 10^{-4}\ \text{s}^{-1}$ for the M_2 tide, $f = (-4.3 \times 10^{-5}, -7.3 \times 10^{-5})\ \text{s}^{-1}$, and $N_b = (6 \times 10^{-4}, 1 \times 10^{-3})\ \text{s}^{-1}$, for the EPR and MAR sites respectively. These bottom values of buoyancy frequency were taken from the data in Fig. 5, not from the exponential fits to the profiles. Tidal current amplitudes of 0.008 m s^{-1} (EPR) and 0.026 m s^{-1} (MAR) were used to calculate the XFZ spectra, which are shown in Fig. 6. Estimated equivalent mode numbers from (6) are given along the upper axes. Spectra from both EPR and MAR sites are ''blue'' with a dependence that is roughly $k^{3/2}$ at low wavenumbers and ''red'' with a dependence that is roughly k^{-2}–k^{-3} for the high wavenumbers. The spectral peaks occur near mode 8 in the EPR data, and near mode 5 in the MAR data.

The integrated energy flux of these XFZ spectra are roughly 0.2 and 4.3 mW m^{-2} for the EPR and MAR sites respectively. Integrated energy flux levels for the FZ sections were roughly 0.1 mW m^{-2} (EPR) and 5.7 mW m^{-2} (MAR). Bathymetric variance levels for different sections at a given site exhibit 50% variations, even between adjacent sections. Also, the relative orientation of the tidal ellipse to a given section influences the energy flux estimate significantly because of the dependence of (2) on u_0^2. However, estimates of total energy flux are rather insensitive to the lower and upper limits of integration, as the dominant contributions to the integrals come from the bandwidths around the spectral peaks. Figure 6 shows the cumulative integrated power along the full spectrum of wavenumbers. In both EPR and MAR cases, over two-thirds of the total power occurs in equivalent modes 1–10. Equivalent modes 1–30 contain over 80% of the total power.

The MAR site clearly produces stronger internal tides than the EPR site. This is due to both the MAR's increased topographic roughness and stronger barotropic tides. Some additional details of the internal-tide estimates for the MAR site are listed in Table 1. Estimates

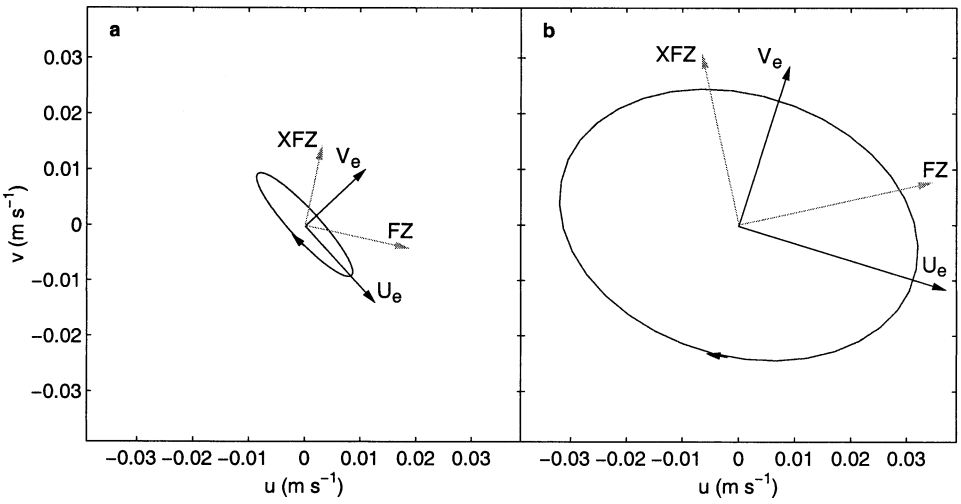

FIG. 4. Tidal ellipses of the barotropic M_2 currents at the (a) EPR and (b) MAR sites. In both cases, the current vectors turn in the clockwise direction over the M_2 tidal period. The axes defined by the semimajor and semiminor currents (U_e, V_e), and the axes aligned with FZ and XFZ directions are also shown.

of root-mean-square (rms) current speeds for various spectral bandwidths were calculated according to Bell's theory,

$$u = \left[\frac{2\omega^2}{\alpha^2}\int^{k'} J_1^2\left(\frac{k'u_0}{\omega}\right)\phi(k')\,dk'\right]^{1/2}. \qquad (7)$$

For example, the rms current associated with equivalent mode 1 was calculated by integrating (7) over the bandwidth $\frac{1}{2}k_1 < k < (3/2)k_1$. The estimates in Table 1 show that for equivalent modes greater than 30, the rms current of the internal tide is comparable to the barotropic current. This demonstrates that the applicability of subcritical theory breaks down at high equivalent modes.

2) TOPOGRAPHY IN TWO DIMENSIONS

Here, we consider the energy flux calculation for topography that varies in both lateral directions. In general, the components of a tidal current can be expressed as $(U, V) = [u_0 \cos(\omega t), v_0 \cos(\omega t + \vartheta)]$, where ϑ is the relative temporal phase between U and V. Llewellyn Smith and Young (2002) have considered this general case. However, for a given tidal ellipse, the semimajor and semiminor current components can be expressed as $(U_e, V_e) = [u_e \cos(\omega t), v_e \sin(\omega t)]$. All phase information is absorbed into the tidal ellipse parameters such that the semimajor and semiminor components are exactly out of phase (Godin 1972). In this reference frame, sub-

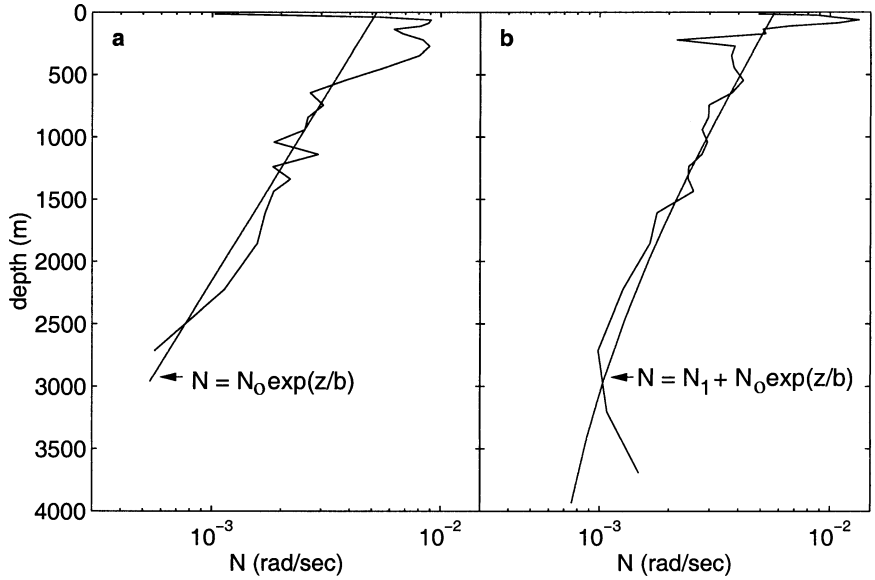

FIG. 5. Profiles of buoyancy frequency N from the (a) EPR and (b) MAR sites. Approximate exponential fits to the data are shown.

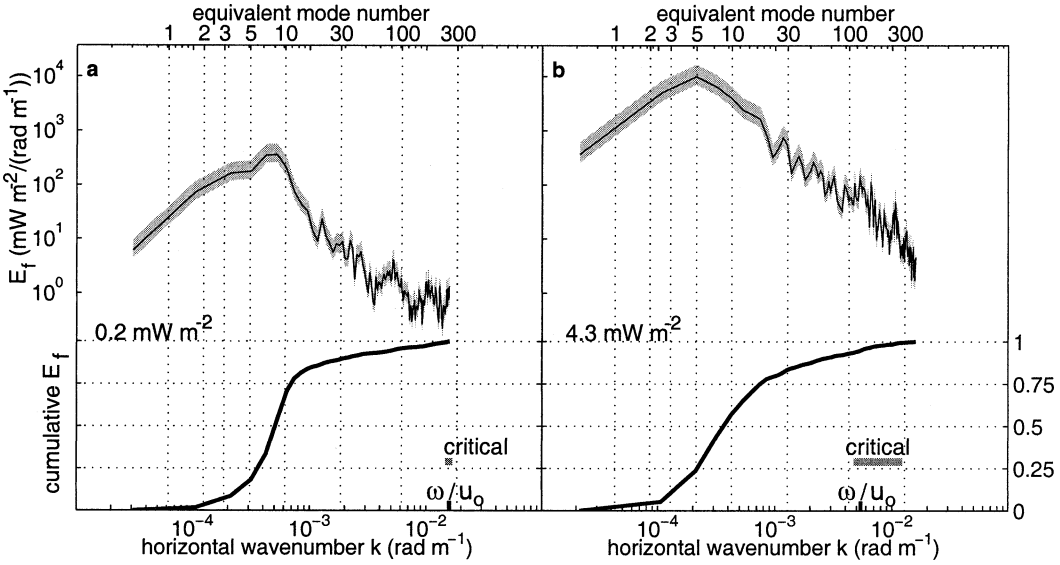

FIG. 6. Energy flux spectra from the (a) EPR and (b) MAR sites. Standard deviations of the spectral estimates are indicated by the shaded bands. For each site, the wavenumber range for critical slopes and the tidal excursion scale are indicated. The cumulative integrals of energy flux are also shown. The equivalent modes are given along the upper axes for reference.

critical theory allows the bottom boundary condition for the vertical velocity to be expressed as

$$w(-H) = u_e \cos(\omega t)\frac{\partial h}{\partial x_e} + v_e \sin(\omega t)\frac{\partial h}{\partial y_e}, \qquad (8)$$

where (x_e, y_e) are the coordinates aligned with the semimajor and semiminor axes. Using standard internal wave relations for wave pressure p, or for the vertical group speed c_g, and energy density E_d (e.g., Gill 1982, 258–267), the vertical energy flux can be expressed as

$$E_f = \rho_0 \frac{[(N_b^2 - \omega^2)(\omega^2 - f^2)]^{1/2}}{\omega(k^2 + l^2)^{1/2}}\langle w^2 \rangle, \qquad (9)$$

where $\langle \cdot \rangle$ is an average over all components of wave phase. This expression for energy flux is only valid for the internal tide response at length scales much larger than the tidal excursion. The energy flux can be expressed as

$$E_f = \frac{1}{2}\rho_0 \frac{[(N_b^2 - \omega^2)(\omega^2 - f^2)]^{1/2}}{\omega} \times \int_0^{2\pi}\int_{K_1}^{\infty} (u_e^2 \cos^2\theta + v_e^2 \sin^2\theta) K^2 \phi(K, \theta)\, dK\, d\theta. \qquad (10)$$

Here (k, l) are the wavenumbers corresponding to the (x_e, y_e) coordinates, $K = (k^2 + l^2)^{1/2}$ is the total wavenumber, and $\theta = \tan^{-1}(l/k)$. The power spectrum of topography is normalized to satisfy $\int_0^{2\pi}\int_0^{\infty} \phi(K, \theta) K\, dK\, d\theta = \overline{h^2}$.

To evaluate (10), a two-dimensional power spectrum must be defined from bathymetry. The multibeam data previously discussed are inadequate for this purpose because of their nonuniform coverage. Gridded bathymetry data from satellite altimetry and ship sounding records have been prepared by Smith and Sandwell (1997, version 8.2; SS97 hereafter). These data provide full spatial coverage, though at a coarse resolution of roughly 3 km. However, given the red spectrum of internal tide energy flux, the SS97 data are adequate for resolving the spatial scales accounting for most of the energy.

As a means of assessing the quality of spectra computed from the SS97 data for the MAR site (Fig. 2b), we have computed spectra along the same bathymetric sections used with the multibeam data. The SS97 spectra are shown along with multibeam spectra in Fig. 7. The SS97 spectra have been wavenumber averaged with a 3-point running boxcar, and standard error confidence bands are shown. The SS97 data are noisier and more statistically uncertain, as they contain significantly fewer degrees of freedom than the multibeam spectra. How-

TABLE 1. Vertical energy flux and baroclinic currents for the M_2 internal tide calculated for a section of XFZ Mid-Atlantic Ridge topography. A barotropic current amplitude of 0.026 m s^{-1} was used in (2) and (7) for these estimates. Values for other parameters are given in the text.

Integrated bandwidth	Energy flux E_f (mW m^{-2})	Rms current speed (m s^{-1})
All modes	4.25 ± 2	0.020 ± 0.004
Mode 1	0.22	0.0013
Modes 1–5	1.01	0.0036
Modes 1–10	2.42	0.0068
Modes 1–30	3.55	0.0104

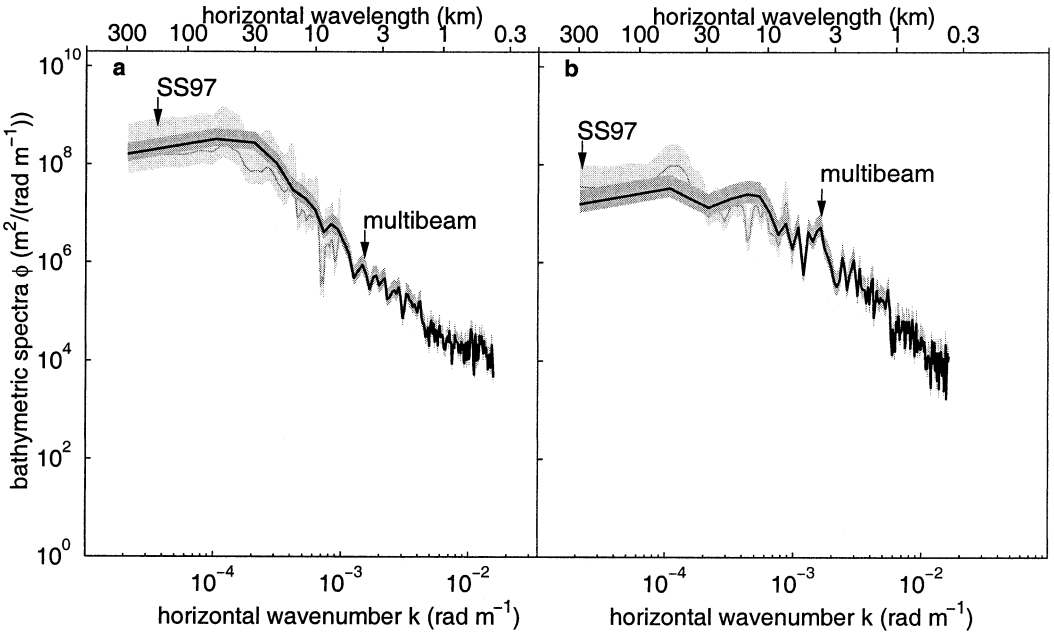

FIG. 7. Spectra of bottom bathymetry from (a) an FZ section and (b) an XFZ section of MAR topography. Spectra were computed from both multibeam data and the gridded SS97 data. Standard errors of the spectra are shown.

ever, the spectra clearly are comparable at the standard error confidence level, and the integrated variance levels out to the SS97 Nyquist wavenumber ($k = 2\pi/6$ km) are within 25%. We note that SS97 data were constrained by the same multibeam data used in this study and in this comparison. Thus, these multibeam sections have strongly influenced the quality of the SS97 spectral estimates for this region.

An estimate of internal tide energy flux from (10) was made for a region of MAR topography between 22° and 32°S and 8° and 20°W (Fig. 8). The region was divided into four sections, and records of barotropic tidal currents were generated using the TPXO.3 model. The M_2 current ellipses were computed in each quadrant (Fig. 8). The semimajor and semiminor axes of each tidal ellipse were used to define a local reference frame, and the SS97 data were regridded to these tidal ellipse coordinates. Power spectra of bathymetry were computed using the tidal ellipse coordinates for each of the four quadrants, and these were used to produce an average spectrum $\phi(k, l)$. An energy flux estimate was made using (10) with $(u_e, v_e) = (0.028, 0.021)$ m s^{-1}, the average semimajor and semiminor current amplitudes of the tidal ellipses shown in Fig. 8. Stratification data from Levitus et al. (1994) and Levitus and Boyer (1994) were used to estimate an average value of $N_b = 8.7 \times 10^{-4}$ s^{-1} for the region. Equivalent modes were identified by substituting the total wavenumber $K_j = (k^2 + l^2)^{1/2}$ into (6), with N_0 and N_1 parameters taken from the fit in Fig. 5b. The average spectrum of energy flux is shown in Fig. 9. We find $E_f = 2.9 \pm 1.3$ mW m^{-2} in the first 25 modes, with the first 10 modes accounting for $E_f = 2.2 \pm 1$ mW m^{-2}. The total area of the region is 1.3×10^{12} m^2, such that 3.8 ± 1.7 GW of internal tide production into equivalent modes 1–25 occurs on average in this region. For comparison, estimates of internal tide production at the Hawaiian Ridge range from 9 to 20 GW (Ray and Mitchum 1997; Egbert and Ray 2000; Merrifield et al. 2001).

Our energy flux estimates along bathymetric sections suggest that equivalent modes 1–25 likely account for 80% of the total vertical energy flux (Fig. 6). Thus, an additional 1 mW m^{-2} may be generated as high equivalent modes. With this addition to our two-dimensional spectral estimate, 4 ± 1 mW m^{-2} is our best estimate of energy flux for this MAR site.

c. Energy flux production at steeper topography

While much of the topography associated with midocean ridge topography is subcritical, small-wavelength features in these regions have increased slopes where the assumptions of subcritical theory are in question. Here, we will make an estimate of the change in efficiency of energy flux production for topographic slopes approaching finite steepness. To do this, we will examine the internal tide generated by a tidal current $U = u_0 \cos\omega t$ along the topography $h = \epsilon\zeta(x)$, where $\zeta(x) = a \cos(kx)$. The small parameter ϵ will serve as the expansion parameter in the perturbation series for the velocity components of the internal tide,

$$w = \epsilon w_1 + \epsilon^2 w_2 + \epsilon^3 w_3 + \cdots, \quad (11)$$

$$u = \epsilon u_1 + \epsilon^2 u_2 + \epsilon^3 u_3 + \cdots, \quad (12)$$

where the subscripts serve as an index. Similar pertur-

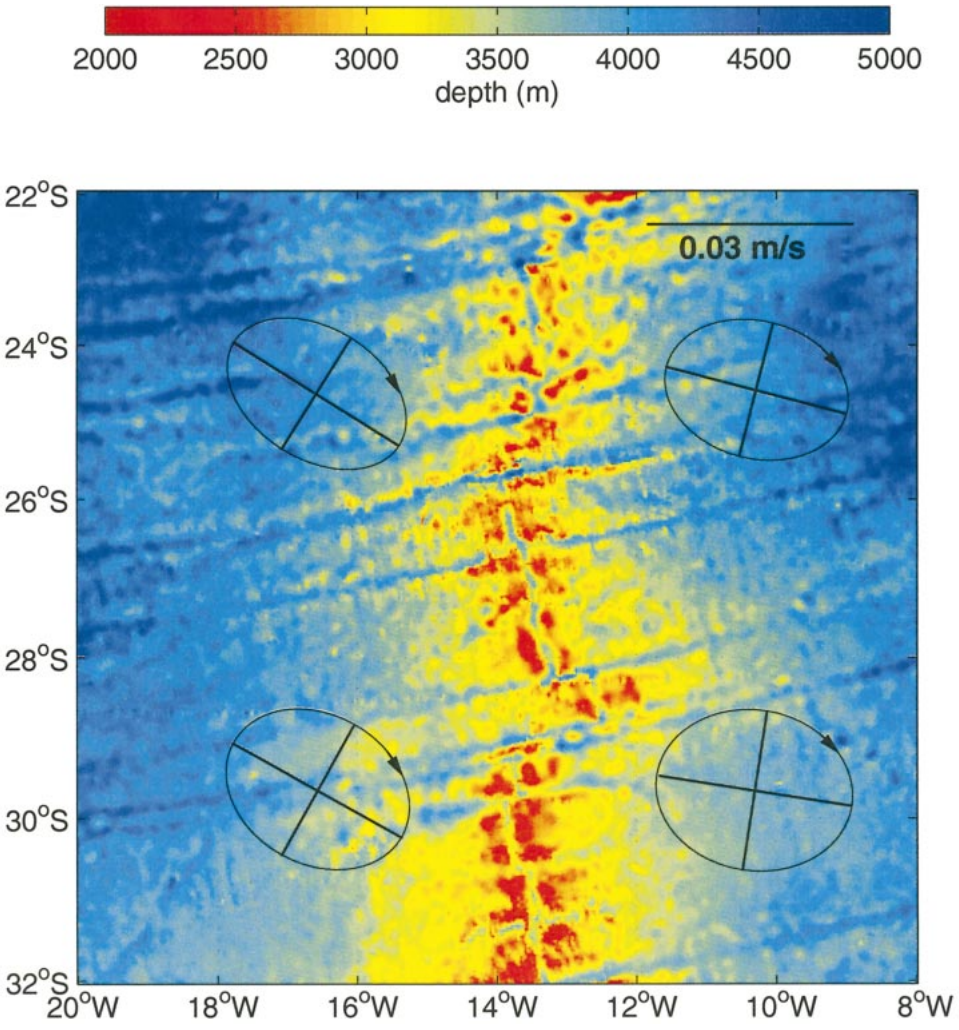

FIG. 8. Map showing the region of MAR topography used in calculations of internal tide energy flux. Tidal ellipses of M_2 currents are also shown.

bation expansions follow for p and ρ in the governing equations

$$\frac{\partial u}{\partial t} = -\frac{1}{\rho_0}\frac{\partial p}{\partial x}, \tag{13}$$

$$\frac{\partial w}{\partial t} = -\frac{1}{\rho_0}\frac{\partial p}{\partial z} - \frac{g}{\rho_0}\rho, \tag{14}$$

$$\frac{\partial \rho}{\partial t} - w\frac{\partial \rho}{\partial z} = 0, \tag{15}$$

$$\frac{\partial u}{\partial x} + \frac{\partial w}{\partial z} = 0. \tag{16}$$

We have neglected advective terms that scale with the temporal rate of change terms as ku_0/ω. This is justified by the assumption that the tidal excursion scale is much less than the scale of the topography, thus limiting this analysis to the internal-tide-regime solution of the governing equations. Quasi-steady lee waves will not be considered here. We seek the solution of (13)–(16) subject to the bottom boundary condition

$$w(h) = (U + u)\frac{\partial h}{\partial x}. \tag{17}$$

We begin by considering Taylor series for the components of the internal tide velocity:

$$w(h) = w(-H) + h\frac{\partial w}{\partial z} + \frac{1}{2}h^2\frac{\partial^2 w}{\partial z^2} + \cdots, \tag{18}$$

$$u(h) = u(-H) + h\frac{\partial u}{\partial z} + \frac{1}{2}h^2\frac{\partial^2 u}{\partial z^2} + \cdots, \tag{19}$$

where all terms are evaluated at $z = -H$, the mean depth of the topography. The bottom boundary condition (17) together with (11), (12), (18), and (19) allows us to write

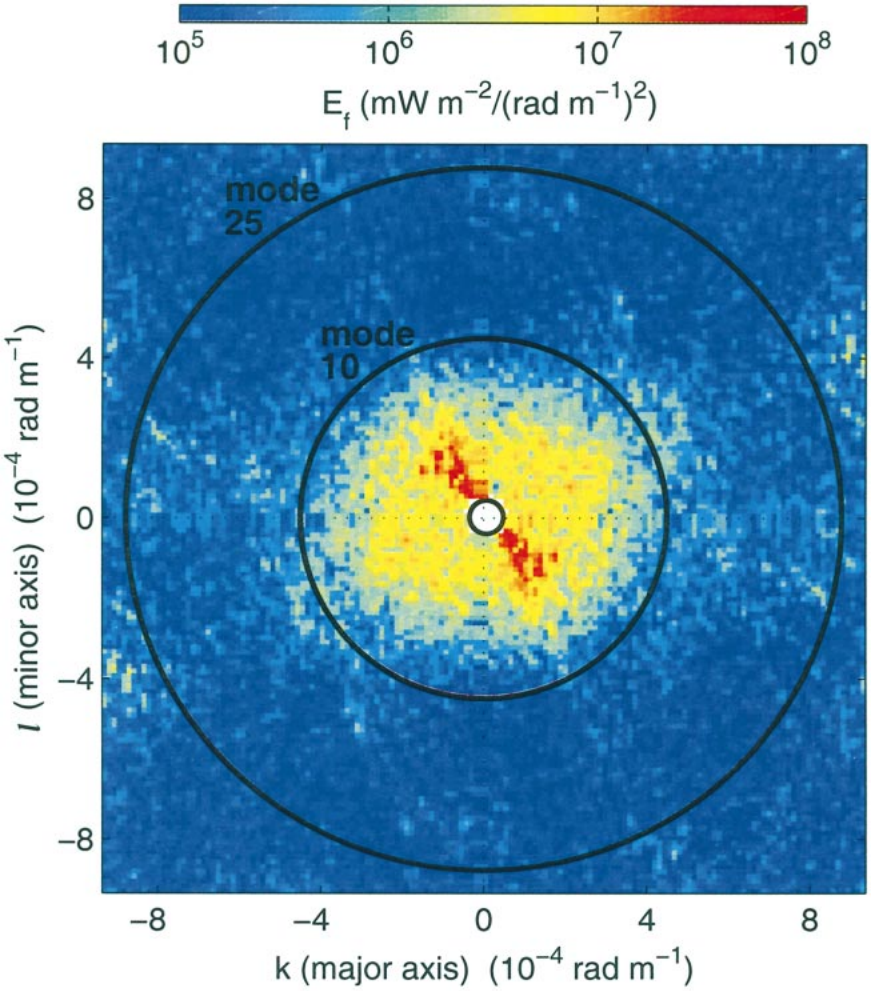

FIG. 9. Two-dimensional spectrum of energy flux in a four-quadrant wavenumber space. The wavenumber axes were taken along the semimajor (k) and semiminor (l) axes of the tidal ellipse reference frame. Circles correspond to the equivalent modes 1, 10, and 25.

$$w_1 = U\frac{\partial \zeta}{\partial x}, \tag{20}$$

$$w_2 = u_1\frac{\partial \zeta}{\partial x} - \zeta\frac{\partial w_1}{\partial z}, \tag{21}$$

$$w_3 = u_2\frac{\partial \zeta}{\partial x} + \zeta\frac{\partial u_1}{\partial z}\frac{\partial \zeta}{\partial x} - \zeta\frac{\partial w_2}{\partial z} - \frac{1}{2}\zeta^2\frac{\partial^2 w_1}{\partial z^2}, \tag{22}$$

and so on for higher-order terms. The first-order solution satisfies the linearized form of the bottom boundary condition,

$$w_1 = -aku_0 \sin kx \cos(mz + \omega t), \tag{23}$$

where $m = kN/\omega$ is the vertical wavenumber of the radiated internal tide. Higher-order corrections follow as

$$w_2 = -a^2 kmu_0 \sin 2kz \sin(2mz + \omega t), \tag{24}$$

$$w_3 = \frac{1}{8}a^3 km^2 u_0[\sin kx \cos(mz + \omega t) + 9 \sin 3kx \cos(3mz + \omega t)]. \tag{25}$$

The vertical energy flux is

$$E_f = \epsilon^2\langle p_1 w_1\rangle + \epsilon^4\langle p_2 w_2 + p_1 w_3 + p_3 w_1\rangle + \cdots = E_{f_1} + E_{f_2} + O(\epsilon^6), \tag{26}$$

where the $\langle\cdot\rangle$ operation is an average over all components of the wave phase. Here, we have defined the E_{f_n} terms such that each includes a factor ϵ^{2n}. Extending the series in (26) to additional higher-order corrections becomes algebraically tedious, as each successive nth correction requires correction of p and w to order $(2n - 1)$. However, the first two terms for the energy flux

follow easily from (23)–(25) along with the corresponding terms in the perturbation series for p,

$$E_{f_1} = \frac{1}{4}\rho_0 kNu_0^2\epsilon^2 a^2, \tag{27}$$

$$E_{f_2} = \frac{1}{16}\rho_0 kNu_0^2 m^2\epsilon^4 a^4. \tag{28}$$

Rewriting (28) using the relation for the aspect ratio of the internal tide beam, $\alpha = k/m$, we have

$$E_{f_2} = \frac{1}{4}\left(\frac{s}{\alpha}\right)^2 E_{f_1}, \tag{29}$$

where $s = \epsilon ka$ is the slope of the topography. The parameter s/α is the slope parameter discussed in section 2.

We have presented the perturbation expansion of energy flux (26) as a means of assessing the change in efficiency of power production as topographic slopes of increasing steepness are considered. Higher-order corrections are clearly necessary to accurately assess the true change in energy flux for topography with finite steepness. However, we find the first correction is a rather small adjustment to the linear solution. We therefore suggest that the energy flux prediction of subcritical theory provides a useful estimate of internal tide power for general topographic slopes with $s < \alpha$. This conclusion is supported by the work of Balmforth et al. (2002), who have extended the series in (26) using MAPLE. They find a convergent series for the case of sinusoidal topography with maximum steepness satisfying the critical condition $s/\alpha = 1$, predicting a 56% increase in the energy flux production over the linear solution. Balmforth et al. also consider the case of a Gaussian seamount, finding only a 14% increase in energy flux over the linear prediction. The numerical results of Li (2002, manuscript submitted to *J. Mar. Res.*) indicate a 70% increase over the linear prediction of energy flux for critical sinusoidal topography. For supercritical slopes, Li finds that a reduction in the buoyancy stratification inhibits the generation of internal tides, with a significant decrease in energy flux, though this result is sensitive to the model's dissipation scheme. Khatiwala (2002, manuscript submitted to *Deep-Sea Res.*) also finds reduced energy-flux production at supercritical topography. Further research on supercritical generation is needed.

3. Discussion

a. Shear instability

Once generated, a beam of internal-tide energy will radiate off the bottom and away from the generation site. The radiated internal tide will be stable to shear (u_z) if the Richardson number ($\mathrm{Ri} = N^2/u_z^2$) is greater than unity at all depths. The shear stability of the radiated internal tide (in isolation from other currents with shear) can be computed for the case of subcritical topography by integrating a function of the bathymetric spectrum $\phi(k)$. An expression for the Richardson number's dependence on vertical wavenumber (m) follows from (7),

$$\mathrm{Ri}(m') = N^2\left[\frac{2\omega^2}{\alpha}\int^{m'} m^2 J_1^2\left(\frac{\alpha m u_0}{\omega}\right)\phi(\alpha m)\, dm\right]^{-1}, \tag{30}$$

where the expression in brackets is an integral over the spectrum of shear for the internal tide of fundamental frequency. Figure 10 shows the Richardson number computed using (30) with the XFZ bathymetry spectra shown in Fig. 3. For the case of internal tides above the EPR, the estimated Richardson number exceeds unity at all vertical wavelengths larger than $O(10)$ m. Internal tides above the MAR site have larger shear, with $\mathrm{Ri} \simeq 1$ at a vertical scale of $m^{-1} \simeq 10$ m, or an equivalent mode of 300. For these high modes, the influence of critical topography during internal-tide generation is likely significant, and our estimates of Ri at high modes are rather questionable. However, we have estimated that such high-mode waves carry a negligible amount of the internal-tide energy flux. Thus, very little internal tide power is likely to dissipate by shear instability immediately after generation from midocean ridge topography.

Observations by Lueck and Mudge (1997) and Lien and Gregg (2001) suggest that higher levels of shear and turbulence occur at sites of internal-tide generation by supercritical topography. At these sites, observed levels of dissipation may be the result of shear instability. However, this local dissipation may represent only a small fraction of the radiated internal-tide energy. For example, recent observations at the Mendocino Escarpment and at Hawaiian Ridge suggest that dissipation near the topography is about 10% of the energy flux radiated away as low-mode internal tides (E. Kunze 2002, personal communication).

To examine the potential for enhanced internal-tide shear at topographic slopes of finite steepness, we again consider the perturbation series solution for waves generated by tidal flow over $h(x) = \epsilon a\cos(kx)$ topography. The first three terms in the series for shear are given by

$$\epsilon\frac{\partial u_1}{\partial z} = \epsilon a m^2 u_0 \cos kx\cos(mz + \omega t), \tag{31}$$

$$\epsilon^2\frac{\partial u_2}{\partial z} = 2\epsilon^2 a^2 m^3 u_0 \cos 2kx\sin(2mz + \omega t), \tag{32}$$

$$\epsilon^3\frac{\partial u_3}{\partial z} = -\frac{1}{8}\epsilon^3 a^3 m^4 u_0[\cos kx\cos(mz + \omega t) + 27\cos 3kx\cos(3mz + \omega t)]. \tag{33}$$

To examine changes in the stability of the internal tide to shear, we must consider corrections to mean square shear S^2 to calculate the Richardson number

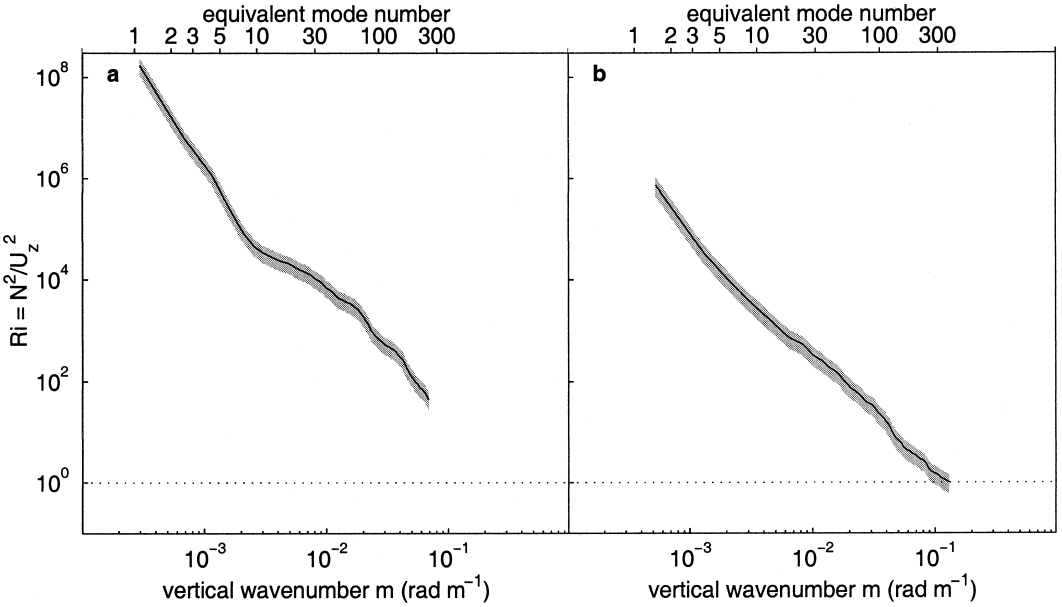

FIG. 10. Vertical wavenumber dependence of the Richardson number for internal tides at the (a) EPR and (b) MAR sites. The standard deviations of the Richardson number estimates are indicated by the shaded bands. Equivalent modes are given along the upper axes for reference.

$$\mathrm{Ri} = \left(N^2 - \epsilon \frac{g}{\rho_0} \frac{\partial \rho_1}{\partial z} - \cdots \right) \Big/ S^2. \tag{34}$$

We will neglect the first correction to the stratification, as $-\epsilon(g/\rho_0)\partial\rho_1/\partial z$ can be shown to be insignificant compared to the background stratification N^2 when $ku_0/\omega \ll 1$. From (31)–(33), the series expansion for the mean square shear follows as

$$\begin{aligned} S^2 &= \epsilon^2 \left\langle \left(\frac{\partial u_1}{\partial z} \right)^2 \right\rangle + \epsilon^4 \left\langle \left(\frac{\partial u_2}{\partial z} \right)^2 + 2 \frac{\partial u_1}{\partial z} \frac{\partial u_3}{\partial z} \right\rangle + \cdots, \\ &= S_1^2 + S_2^2 + O(\epsilon^6), \end{aligned} \tag{35}$$

where the S_n^2 terms are the nth-order contributions to the mean square shear. The first two contributions to the mean square shear are

$$S_1^2 = \frac{1}{4} \epsilon^2 a^2 m^4 u_0^2, \tag{36}$$

$$S_2^2 = \frac{15}{4} \left(\frac{s}{\alpha} \right)^2 S_1^2. \tag{37}$$

It follows that the first correction to S^2 accounting for increased steepness is rather significant. For $s/\alpha = 1/2$, the first correction is a 94% increase in the mean square shear. This gives nearly a 50% reduction in the Richardson number.

b. Wave–wave interactions

The transfer of energy between wave modes due to wave–wave interactions has been the subject of a number of studies (e.g., McComas and Müller 1981a,b; Henyey et al. 1986; Hirst 1991, 1996), and a review of this subject was given by Müller et al. (1986). Olbers and Pomphrey (1981) and Hirst (1996) specifically examined the wave–wave interactions between the internal tide and the internal wave continuum and estimated the timescale for the energy transfer away from modes 1–10 to higher modes. They considered the Parametric Subharmonic Instability (PSI) resonant interaction, which transfers tidal energy with frequency ω to larger vertical wavenumbers with frequency $\omega/2$. Thus, the PSI mechanism is an effective mechanism for dissipating the M_2 internal tides at latitudes less than about 30°. Estimates of the dissipation timescale for the M_2 internal tides by PSI are given in Fig. 11 (adapted from Olbers 1983). The transfer timescale is $O(100)$ days for mode 1, consistent with the observed slow southward decay of low-mode internal tides generated at the Hawaiian Ridge (Ray and Mitchum 1996) and Aleutian Ridge (Cummins et al. 2001). The PSI transfer timescale decreases to $O(1)$ day for mode 10. Hirst (1996) also discusses conditions where strong tidal forcing can result in reduced transfer timescales for low-mode internal tides.

Most other studies have considered the additional resonant interactions occurring in the general internal wave continuum over the range of frequencies between f and N. The ''elastic scattering'' and ''induced diffusion'' interactions may influence internal tides at all latitudes. In all cases, wave interaction timescales for low modes with tidal frequencies typically exceed $O(10)$ days (Müller et al. 1986; Hirst 1991).

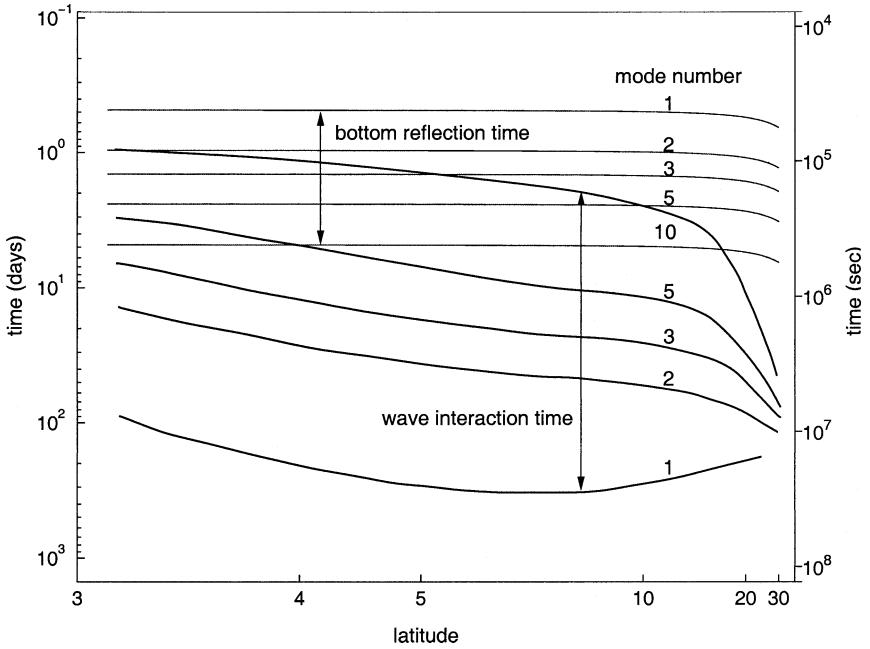

FIG. 11. The timescales for wave–wave (PSI) interactions between the M_2 internal tide and the internal wave continuum for modes 1, 2, 3, 5, and 10, adapted from Olbers (1983). The PSI interaction for the M_2 tide occurs equatorward of $\pm 30°$ lat. Bottom reflection times for the various modes were estimated for an exponential stratification over a depth of 4000 m.

It is useful to compare the wave interaction timescale to the time for a wave group to travel from bottom to surface and back again, defined according to

$$\tau_g = 2\int c_g^{-1}\, dz,$$

where the integral is over the ocean depth and c_g is the vertical component of the group speed. The latitude and mode-number-dependent curves for τ_g were computed using $N = N_0 e^{z/b}$ with $(b, N_0) = (1300\text{ m}, 0.005\,24\text{ s}^{-1})$, and the results are shown in Fig. 11. Low modes have the fastest group speeds, with $\tau_g \leq 12$ h for mode 1 and $\tau_g \geq 4$ days for mode 10. Thus, low modes will easily complete one round-trip between the bottom and surface before experiencing the effects of wave–wave interactions. For modes $j \geq 10$, energy transfer to higher modes will occur over a timescale comparable to, or faster than, the bottom reflection time. Thus, wave–wave interactions may be the dominant mechanism of spectral evolution for high-mode components of the internal tide, while bottom reflection is significant for low modes.

c. Bottom reflection and topographic scattering

The interaction of internal waves with bottom bathymetry is often discussed in terms of wave reflection from sloping topography and wave scattering from rough topography. Particular attention has been given to reflection from planar slopes (e.g., Eriksen 1982, 1985; Garrett and Gilbert 1988; Thorpe 1987, 1997, 1999). Reflection from slopes with nonplanar geometries has been considered by Gilbert and Garrett (1989) and Müller and Liu (2000a,b). Scattering of waves from random rough topography was considered by Müller and Xu (1992), and Thorpe (2001) considered scattering from rough topography with an underlying slope. For the midocean ridge topography discussed in section 2b, the latter studies are clearly most relevant.

As discussed by Müller and Xu (1992), both reflection and scattering redistribute energy flux in wavenumber space. Müller and Xu (1992) find that scattering is more efficient than reflection at redistributing energy flux to higher modes, particularly at tidal and near-inertial frequencies. However, Müller and Xu (1992) find less than 10% of the incoming radiation is redistributed during a scattering event at typical deep-ocean topography. Most of the incoming radiation undergoes pure reflection as from a flat bottom, such that the wavenumber content of the spectrum is mostly preserved.

Here, we consider the similarity between internal-tide generation and the scattering of low-mode internal tides. In this simple calculation, we exploit the fact that the wave response to a mode-1 current flowing over small topographic wavelengths is much the same as the wave response to a barotropic current. We will examine the scattering of the mode-1 internal tide through a ''second generation'' calculation, where the amplitude of the mode-1 current is used in place of the amplitude of the barotropic current in (2). This is meant to provide a crude estimate of the energy flux scattered from mode 1 into higher modes. The rms current for the mode-1 internal tide at the MAR site was found to be $u = 0.0013$

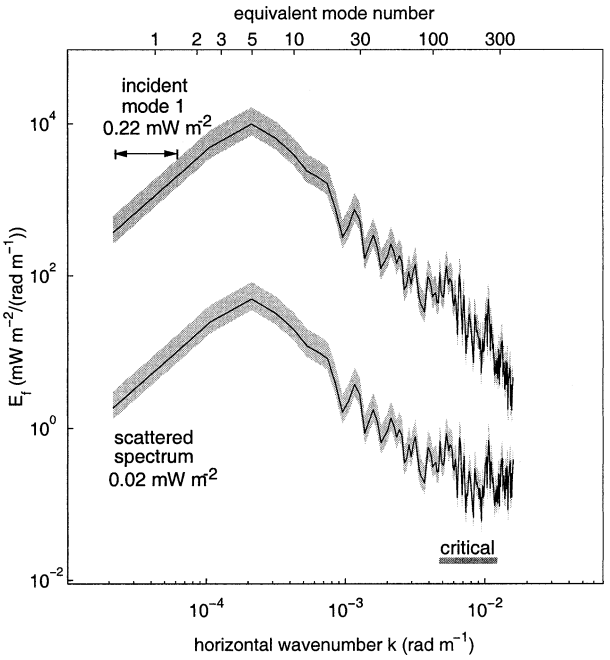

FIG. 12. Spectra of incident and scattered mode-1 energy flux from MAR bathymetry. The wavenumber range associated with critical slopes is shown.

m s^{-1} (Table 1), corresponding to a current amplitude of $\sqrt{2}u = 0.0018$ m s^{-1}. The incident and scattered spectra of energy flux are shown in Fig. 12. The resulting estimate of scattered energy flux, integrated over all scattered wavenumbers, is roughly 0.023 mW m^{-2}. This compares to an incident mode-1 energy flux of roughly 0.22 mW m^{-2}. Thus, we find mode-1 scattering occurs with an efficiency of about 10%, comparable to the efficiencies estimated by Müller and Xu (1992). We note that in our estimate, a small amount of scattered energy flux is predicted in the lowest several modes, so our scattering efficiency is a bit high.

4. Conclusions

Having considered the various mechanisms that can act to degrade the internal tides into turbulence, it is possible to speculate about the nature of internal-tide-driven mixing in the deep ocean. Low-mode waves are relatively uninfluenced by wave–wave interactions and their Richardson numbers are large. In regions where additional sheared currents are absent, low modes will propagate away from their generation sites, carrying much of the generated energy flux. The lateral distance for one round-trip between the bottom and surface can be estimated using the characteristic equation for a tidal beam, $dx/dz = \alpha^{-1}$, such that

$$\Delta x = 2 \int_{-H}^{0} \left[\frac{N^2(z) - \omega^2}{\omega^2 - f^2} \right]^{1/2} dz. \qquad (38)$$

For typical stratification in the deep ocean, this radiation distance is $\Delta x \simeq 100$ km. Thus, waves corresponding to low modes can be expected to travel O(100 km) before scattering from topography. During topographic scattering, much of the low-mode energy flux is preserved, suggesting that low modes can radiate through many bottom encounters. Observations of internal tides generated at Hawaii (Ray and Mitchum 1996) and the Aleutian Ridge (Cummins et al. 2001) demonstrate that low modes can be tracked for O(1000) km away from their generation site.

Most internal-tide-driven mixing must be supported by high equivalent modes that have more shear, making them more likely to dissipate locally by shear instability. This is particularly true of internal tides generated at critical slopes, such as those found along supercritical topography. Wave–wave interactions are also more efficient for higher modes, providing another mechanism for converting internal tide energy flux into turbulence. The ''Parametric Subharmonic Instability'' interaction is particularly effective since it specifically moves energy to higher equivalent modes. However, the PSI mechanism for tidal frequencies is only effective at low latitudes. The effectiveness of other classes of wave–wave interactions at transferring wave energy to higher modes is unclear, though some ideas are presented by Polzin (1999).

The wave–wave interaction timescale for equivalent mode 10 is roughly equal to the timescale over which the mode-10 tidal beam completes a round-trip between the bottom and surface. Over this characteristic timescale, the mode-10 tidal beam radiates roughly 100 km from the generation site. Higher equivalent modes will be increasingly influenced by the wave–wave interactions over shorter time- and distance scales. We suggest that for a given internal-tide-generation event, waves with equivalent modes less than 10 are likely to radiate away, with equivalent modes greater than 10 dissipating locally. For the MAR topography considered in section 2b, this suggests that roughly one-third of the generated power, about 1–2 mW m^{-2}, may dissipate as turbulence at this site. At other sites, the amount of energy flux available in equivalent modes greater than 10 will clearly depend on the nature of the topography, and the nature of the barotropic tides. As shown in section 2b, the energy flux production at site along the EPR is only 0.2 mW m^{-1}.

Low equivalent modes that radiate away will be influenced by topographic scattering. Energy scattered to higher modes is more likely to dissipate, so topographic scattering provides a mechanism for driving mixing away from an internal-tide-generation site. However, the efficiency of topographic scattering is low, with roughly 10% of low-mode energy flux being transferred to higher modes. It is possible that while the scattering efficiency for general topographies is low, certain topographic sites may favor enhanced scattering. For example, Gilbert and Garrett (1989) and Müller and Liu (2000b) find convex topographies are more efficient

than linear or concave topographies at scattering energy to high modes. Thus, in addition to the internal tides generated at such sites, convex topographies may be favored sites for the dissipation of incoming internal-tide energy. At such sites, the scattered waves could act as a catalyst for dissipating the locally generated waves since elevated shear levels in the scattered waves will contribute to a lower overall Richardson number.

Given the inefficient nature of topographic scattering at general topographies, it is likely that low-mode internal tides radiate much of their energy through multiple bottom reflections over $O(1000$ km) distances. Low modes must dissipate somewhere, but the nature of low-mode dissipation is particularly unclear. Perhaps low modes are preferentially dissipated in regions of enhanced sheared currents, such as the equatorial undercurrents or the Antarctic Circumpolar Current. Perhaps low modes propagate onto the continental shelves where they dissipate in shallow waters. Finally, perhaps low modes are dissipated throughout in the interior of the deep ocean under the slow evolution of wave–wave interactions. In this scenario, much of the energy in low-mode internal tides would be uniformly dispersed through the oceanic interior. The dissipation of this energy would contribute to background levels of turbulence everywhere. The fate of low-mode internal tides, however, remains as a primary question.

Acknowledgments. We thank Eric D'Asaro, Eric Kunze, and Bill Young for carefully reviewing the manuscript. We also thank Gary Egbert, Ming Li, Stefan Llewellyn Smith, Kurt Polzin, and John Toole for helpful discussions about this work. Multibeam bathymetry data were obtained from the RIDGE Multibeam Synthesis Project. Comments and suggestions from two anonymous reviewers also improved this presentation. The authors were supported by the U.S. Office of Naval Research and the Natural Science and Engineering Research Council of Canada.

REFERENCES

Baines, P. G., 1973: The generation of internal tides by flat-bump topography. *Deep-Sea Res.,* **20,** 179–205.

——, 1982: On internal tide generation models. *Deep-Sea Res.,* **29,** 307–338.

Balmforth, N. J., G. R. Ierley, and W. R. Young, 2002: Tidal conversion by subcritical topography. *J. Phys. Oceanogr.,* **32,** 2900–2914.

Bell, T. H., 1975a: Lee waves in stratified flows with simple harmonic time dependence. *J. Fluid Mech.,* **67,** 705–722.

——, 1975b: Topographically generated internal waves in the open ocean. *J. Geophys. Res.,* **80,** 320–327.

Cox, C. S., and H. Sandstrom, 1962: Coupling of surface and internal waves in water of variable depth. *J. Oceanogr. Soc. Japan*, 20th Anniversary Volume, 499–513.

Craig, P. D., 1987: Solutions for internal tide generation over coastal topography. *J. Mar. Res.,* **45,** 83–105.

Cummins, P. F., J. Y. Cherniawski, and M. G. G. Foreman, 2001: North Pacific internal tides from the Aleutian Ridge: Altimeter observations and modelling. *J. Mar. Res.,* **59,** 167–191.

Egbert, G. D., 1997: Tidal data inversion: Interpolation and inference. *Progress in Oceanography*, Vol. 40, Pergamon, 81–108.

——, and R. D. Ray, 2000: Significant dissipation of tidal energy in the deep ocean inferred from satellite altimeter data. *Nature,* **405,** 775–778.

——, and ——, 2001: Estimates of M_2 tidal energy dissipation from TOPEX/POSEIDON altimeter data. *J. Geophys. Res.,* **106,** 22 475–22 502.

——, A. F. Bennett, and M. G. G. Foreman, 1994: TOPEX/POSEIDON tides estimated using a global inverse model. *J. Geophys. Res.,* **99,** 24 821–24 852.

Eriksen, C., 1982: Observations of internal wave reflection off sloping bottoms. *J. Geophys. Res.,* **87,** 525–538.

——, 1985: Implications of ocean bottom reflection for internal wave spectra and mixing. *J. Phys. Oceanogr.,* **15,** 1145–1156.

Garrett, C., and D. Gilbert, 1988: Estimates of vertical mixing by internal waves reflected off sloping topography. *Small-Scale Turbulence and Mixing in the Ocean*. J. C. J. Nihoul and B. M. Janard, Eds., Elsevier Scientific, 405–424.

Gilbert, D., and C. Garrett, 1989: Implications for ocean mixing of internal waves scattering off irregular topography. *J. Phys. Oceanogr.,* **19,** 1716–1729.

Gill, A. E., 1982: *Atmosphere–Ocean Dynamics*. Academic Press, 662 pp.

Godin, G., 1972: *The Analysis of Tides*. University of Toronto Press, 264 pp.

Goff, J. A., 1991: A global and regional stochastic analysis of near-ridge abyssal hill morphology. *J. Geophys. Res.,* **96,** 21 713–21 737.

Hendershott, M. C., 1981: Long waves and ocean tides. *Evolution of Physical Oceanography*, B. A. Warren and C. Wunsch, Eds., The MIT Press, 292–341.

Henyey, F. S., J. Wright, and S. M. Flatté, 1986: Energy and action flow through the internal wave field: An eikonal approach. *J. Geophys. Res.,* **91,** 8487–8495.

Hibiya, T., 1986: Generation mechanism of internal waves by tidal flow over a sill. *J. Geophys. Res.,* **91,** 7696–7708.

Hirst, E., 1991: Internal wave–wave resonance theory: Fundamentals and limitations. *Dynamics of Oceanic Internal Gravity Waves*: *Proc. 'Aha Huliko' a Hawaiian Winter Workshop*, P. Müller and D. Henderson, Eds., Honolulu, HI, University of Hawaii at Manoa, 211–226.

——, 1996: Resonant instability of internal tides. Ph. D. dissertation, University of Washington, 92 pp.

Holloway, P. E., and M. A. Merrifield, 1999: Internal tide generation by seamounts, ridges and islands. *J. Geophys. Res.,* **104,** 25 937–25 951.

Kunze, E., and J. M. Toole, 1997: Tidally driven vorticity, diurnal shear, and turbulence atop Fieberling Seamount. *J. Phys. Oceanogr.,* **27,** 2663–2693.

Ledwell, J. R., E. T. Montgomery, K. L. Polzin, L. C. St. Laurent, R. W. Schmitt, and J. M. Toole, 2000: Mixing over rough topography in the Brazil Basin. *Nature,* **403,** 179–182.

Levitus, S., and T. P. Boyer, 1994: *Temperature*. Vol. 4, *World Ocean Atlas 1994*, NOAA Atlas NESDIS 4, 117 pp.

——, R. Burgett, and T. Boyer, 1994: *Salinity*. Vol. 3, *World Ocean Atlas 1994*, NOAA Atlas NESDIS 3, 99 pp.

Lien, R.-C., and M. C. Gregg, 2001: Observations of turbulence in a tidal beam and across a coastal ridge. *J. Geophys. Res.,* **106,** 4575–4592.

Llewellyn Smith, S. G., and W. R. Young, 2002: Conversion of the barotropic tide. *J. Phys. Oceanogr.,* **32,** 1554–1566.

Lott, F., and H. Teitelbaum, 1993: Linear unsteady mountain waves. *Tellus,* **45,** 201–220.

Lueck, R. G., and T. D. Mudge, 1997: Topographically induced mixing around a shallow seamount. *Science,* **276,** 1831–1833.

McComas, C. H., and P. Müller, 1981a: The dynamic balance of internal waves. *J. Phys. Oceanogr.,* **11,** 970–986.

——, and ——, 1981b: Time scales of resonant interactions among oceanic internal waves. *J. Phys. Oceanogr.,* **11,** 139–147.

Merrifield, M. A., P. E. Holloway, and T. M. Shaun Johnston, 2001:

The generation of internal tides at the Hawaiian Ridge. *Geophys. Res. Lett.,* **28,** 559–562.

Müller, P., and N. Xu, 1992: Scattering of oceanic internal waves off random bottom topography. *J. Phys. Oceanogr.,* **22,** 474–488.

——, and X. Liu, 2000a: Scattering of internal waves at finite topography in two dimensions. Part I: Theory and case studies. *J. Phys. Oceanogr.,* **30,** 532–549.

——, and ——, 2000b: Scattering of internal waves at finite topography in two dimensions. Part II: Spectral calculations and boundary mixing. *J. Phys. Oceanogr.,* **30,** 550–563.

——, G. Holloway, F. Henyey, and N. Pomphrey, 1986: Nonlinear interactions among internal gravity waves. *Rev. Geophys.,* **24,** 493–536.

Munk, W., and C. Wunsch, 1998: Abyssal recipes II: Energetics of tidal and wind mixing. *Deep-Sea Res.,* **45,** 1977–2010.

Nakamura, T., T. Awaji, T. Hatayama, and K. Akitomo, 2000: The generation of large amplitude unsteady lee waves by subinertial K_1 tidal flow: A possible vertical mixing mechanism in the Kuril Straits. *J. Phys. Oceanogr.,* **30,** 1601–1621.

Olbers, D. J., 1983: Models of the oceanic internal wave field. *Rev. Geophys.,* **21,** 1567–1606.

——, and N. Pomphrey, 1981: Disqualifying two candidates for the energy balance of oceanic internal waves. *J. Phys. Oceanogr.,* **11,** 1423–1425.

Polzin, K. L., 1999: A rough recipe for the energy balance of quasi-steady internal lee waves. *Dynamics of Oceanic Internal Gravity Waves, II: Proc. 'Aha Huliko'a Hawaiian Winter Workshop,* P. Müller and D. Henderson, Eds., Honolulu, HI, University of Hawaii at Manoa, 117–128.

——, J. M. Toole, J. R. Ledwell, and R. W. Schmitt, 1997: Spatial variability of turbulent mixing in the abyssal ocean. *Science,* **276,** 93–96.

Rattray, M., 1960: On the coastal generation of internal tides. *Tellus,* **12,** 54–61.

Ray, R., and G. T. Mitchum, 1996: Surface manifestation of internal tides generated near Hawaii. *Geophys. Res. Lett.,* **23,** 2101–2104.

——, and ——, 1997: Surface manifestation of internal tides in the deep ocean: Observations from altimetry and island gauges. *Progress in Oceanography,* Vol. 40, Pergamon, 135–162.

Seibold, E., and W. H. Berger, 1996: *The Sea Floor—An Introduction to Marine Geology*. Springer-Verlag, 356 pp.

Sjöberg, B., and A. Stigebrandt, 1992: Computations of the geographical distribution of the energy flux to mixing processes via internal tides and the associated vertical circulation in the ocean. *Deep-Sea Res.,* **39,** 269–291.

Small, C., and D. Sandwell, 1992: An analysis of ridge axis gravity roughness and spreading rate. *J. Geophys. Res.,* **97,** 3235–3245.

Smith, W. H. F., and D. T. Sandwell, 1997: Global sea floor topography from satellite altimetry and ship depth soundings. *Science,* **277,** 1956–1962.

Stigebrandt, A., 1980: Some aspects of tidal interaction with Fjord Constrictions. *Estuarine Coastal Mar. Sci.,* **11,** 151–166.

St. Laurent, L. C., J. M. Toole, and R. W. Schmitt, 2001: Buoyancy forcing by turbulence above rough topography in the abyssal Brazil Basin. *J. Phys. Oceanogr.,* **31,** 3476–3495.

Thorpe, S. A., 1987: On the reflection of a train of finite amplitude waves from a uniform slope. *J. Fluid Mech.,* **178,** 279–302.

——, 1997: On the interactions of internal waves reflecting from slopes. *J. Phys. Oceanogr.,* **27,** 2072–2078.

——, 1999: Fronts formed by obliquely reflecting internal waves at a sloping boundary. *J. Phys. Oceanogr.,* **29,** 29–38.

——, 2001: Internal wave reflection and scatter from sloping rough topography. *J. Phys. Oceanogr.,* **31,** 537–553.

Wunsch, C., 1975: Internal tides in the ocean. *Rev. Geophys.,* **13,** 167–182.